Geophysical Journal International

*Geophys. J. Int.* (2016) **204,** 1636–1648 doi: 10.1093/gji/ggv542
GJI Seismology

# Crustal and upper-mantle structure beneath ice-covered regions in Antarctica from *S*-wave receiver functions and implications for heat flow

C. Ramirez,[1] A. Nyblade,[1] S.E. Hansen,[2] D.A. Wiens,[3] S. Anandakrishnan,[1] R.C. Aster,[4] A.D. Huerta,[5] P. Shore[3] and T. Wilson[6]

[1]*Department of Geosciences, The Pennsylvania State University; University Park, PA* 16802, *USA. E-mail: crsito_15@yahoo.com*
[2]*Department of Geosciences, The University of Alabama, Tuscaloosa, AL* 35487, *USA*
[3]*Department of Earth and Planetary Sciences, Washington University, St. Louis, MO* 63130, *USA*
[4]*Department of Geosciences, Colorado State University, Fort Collins, CO* 80523, *USA*
[5]*Department of Geological Sciences, Central Washington University, Ellensburg, WA* 98926, *USA*
[6]*Byrd Polar Research Center and School of Earth Sciences, The Ohio State University, Columbus, OH* 43210, *USA*

Accepted 2015 December 16. Received 2015 December 7; in original form 2015 August 18

## SUMMARY

*S*-wave receiver functions (SRFs) are used to investigate crustal and upper-mantle structure beneath several ice-covered areas of Antarctica. Moho S-to-P (Sp) arrivals are observed at ∼6–8 s in SRF stacks for stations in the Gamburtsev Mountains (GAM) and Vostok Highlands (VHIG), ∼5–6 s for stations in the Transantarctic Mountains (TAM) and the Wilkes Basin (WILK), and ∼3–4 s for stations in the West Antarctic Rift System (WARS) and the Marie Byrd Land Dome (MBLD). A grid search is used to model the Moho Sp conversion time with Rayleigh wave phase velocities from 18 to 30 s period to estimate crustal thickness and mean crustal shear wave velocity. The Moho depths obtained are between 43 and 58 km for GAM, 36 and 47 km for VHIG, 39 and 46 km for WILK, 39 and 45 km for TAM, 19 and 29 km for WARS and 20 and 35 km for MBLD. SRF stacks for GAM, VHIG, WILK and TAM show little evidence of Sp arrivals coming from upper-mantle depths. SRF stacks for WARS and MBLD show Sp energy arriving from upper-mantle depths but arrival amplitudes do not rise above bootstrapped uncertainty bounds. The age and thickness of the crust is used as a heat flow proxy through comparison with other similar terrains where heat flow has been measured. Crustal structure in GAM, VHIG and WILK is similar to Precambrian terrains in other continents where heat flow ranges from ∼41 to 58 mW $m^{-2}$, suggesting that heat flow across those areas of East Antarctica is not elevated. For the WARS, we use the Cretaceous Newfoundland–Iberia rifted margins and the Mesozoic-Tertiary North Sea rift as tectonic analogues. The low-to-moderate heat flow reported for the Newfoundland–Iberia margins (40–65 mW $m^{-2}$) and North Sea rift (60–85 mW $m^{-2}$) suggest that heat flow across the WARS also may not be elevated. However, the possibility of high heat flow associated with localized Cenozoic extension or Cenozoic-recent magmatic activity in some parts of the WARS cannot be ruled out.

**Key words:** Heat flow; Seismicity and tectonics; Site effects; Antarctica.

## 1 INTRODUCTION

The stability of the West Antarctic Ice Sheet (WAIS) and other large glaciers in Antarctica, although of great importance because of their potential to raise sea level by several meters, is poorly understood, in part because there are very few heat flow measurements available for constraining models of ice sheet behaviour (e.g. Parizek 2002; Bennett 2003; Pollard *et al.* 2005; Pattyn 2010; Larour *et al.* 2012). In the absence of direct borehole measurements, one approach to estimating heat flow is to use crustal and upper-mantle structure as a proxy via comparison to tectonically similar regions around the world where heat flow has been measured. Indeed, the use of heat flow from terrains with similar structure and age as a proxy is commonplace (e.g. Pollack *et al.* 1993; Artemieva & Mooney 2001; Pollard *et al.* 2005; Davies & Davies 2010; Davies 2013).

Obtaining estimates of crustal and upper-mantle structure in Antarctica needed for applying this approach, however, can be challenging. Harsh environmental conditions make it difficult to obtain seismic data, especially in the interior of the continent, and where seismic data have been collected, reverberations within the thick ice sheets often make the use of standard data analysis methods for imaging crustal and upper-mantle structure difficult. In particular, reverberations within the ice layer can mask key converted seismic phases from deeper discontinuities, such as the Moho or the lithosphere–asthenosphere boundary (LAB).

In order to improve our understanding of crustal and upper-mantle structure in Antarctica, and to use this understanding for inferring heat flow, *S*-wave receiver functions (SRFs) are modelled together with Rayleigh wave phase velocity measurements to image crustal and upper-mantle structure beneath many broad-band seismic stations deployed on ice. Imaging earth structure beneath glaciers using SRFs can be less complicated than *P*-wave receiver function (PRF) imaging (e.g. Chaput *et al.* 2014) because SRFs do not contain reverberations from the ice layer (Hansen *et al.* 2009a, 2010). SRFs can also often provide information about discontinuities in the upper mantle not apparent in PRFs (e.g. Rychert *et al.* 2005; Hansen *et al.* 2009b; Ford *et al.* 2010).

Here we apply the SRF method systematically to data from seismic stations deployed on ice in Antarctica, incorporating bootstrapped error bounds on the SRF stacks to obtain uncertainty estimates on models of crustal and upper-mantle structure. Results obtained for areas in East Antarctica (EA) and West Antarctica (WA) are then compared to similar terrains in other parts of the globe where heat flow has been measured to comment on heat flow in Antarctica.

## 2 TECTONIC BACKGROUND

Antarctica consists of three first-order tectonic domains: WA, EA and the Transantarctic Mountains (TAM), which separate EA from WA. In this section, the relevant geology and physiography of these regions are briefly reviewed.

### 2.1 West Antarctica

Although WA is composed of several tectonic blocks (Dalziel & Elliot 1982), the data used in this study come from just two of them: the West Antarctic Rift System (WARS) and the Marie Byrd Land Dome (MBLD; Fig. 1). The WARS is one of the most extensive physiographic features in WA (Fig. 1), extending from the Ross Sea to the Antarctic Peninsula, covering a distance of ∼3000 km (Behrendt *et al.* 1991). It is bound to the north and south by the MBLD and the TAM, respectively. The size and tectonic setting of the WARS have been often compared to that of the Cenozoic Basin and Range province in the continental U.S., the Cenozoic East African Rift System, the Mesozoic-Tertiary North Sea Rift, and the Jurassic-Cretaceous Newfoundland–Iberia passive margins (Behrendt *et al.* 1991; Tessensohn & Woörner 1991; Behrendt 1999; LeMasurier 2008). The WARS section between the MBLD and the TAM is referred to as the eastern WARS, and the section in the Ross Sea as the western WARS. The western WARS consists of three basins, the Victoria Land Basin, immediately adjacent to the TAM, and the Central and Eastern Basins outboard to the north. The eastern WARS is characterized topographically by several deep basins, most prominently the Byrd Subglacial Basin and the Bentley Subglacial Trench (Fig. 1).

The initiation of rifting in the WARS is not well known but probably started in the Jurassic when Africa separated from EA, with a primary phase of extension circa 105–85 Ma during the breakup and opening of the Southern Ocean between WA and New Zealand (Behrendt *et al.* 1991; Tessensohn & Woörner 1991; Siddoway 2008). Extension during the Cretaceous rifting phase was >100 per cent, resulting from pure shear deformation orthogonal to the TAM (Siddoway 2008 and references therein). Renewed extension in the Cenozoic within the western WARS has been documented from sea floor spreading in the Adare trough, reconstructions of plate circuits, and the development of the Terror rift within the Victoria Land Basin (Cande & Stock 2004; Müller *et al.* 2007; Stuart *et al.* 2007; Fielding *et al.* 2008; Wilson & Luyendyk 2009; Granot *et al.* 2010), with possibly up to 150 km of extension between 68–46 Ma (Cande & Stock 2004; Wilson & Luyendyk 2009). However, how much of the Cenozoic extension affected the Central and Eastern Basins of the western WARS, as well as the eastern WARS, remains uncertain (e.g. Karner *et al.* 2005), with some studies even predicting compression within the eastern WARS during the Eocene and Oligocene (Granot *et al.* 2010).

Several of the deep basins in the eastern WARS (e.g. Byrd Subglacial Basin, the Bentley Subglacial Trench and the Pine Island trough), which have locally much thinner crust than surrounding areas of the eastern WARS (e.g. Winberry & Anandakrishnan 2004; Chaput *et al.* 2014), have been interpreted as Cenozoic rift basins (e.g. LeMasurier 2008; Jordan *et al.* 2010). A seismic low wave speed anomaly in the upper mantle beneath the Bentley Trench supports that interpretation (Lloyd *et al.* 2015). However, Wannamaker *et al.* (1996) reported high crustal and upper-mantle resistivity values beneath the Byrd basin, suggestive of an inactive rift, and similar deep basins have been imaged beneath the Central and Eastern Basins of the western WARS which show little evidence for Cenozoic extension (Trey *et al.* 1999; Karner *et al.* 2005). There is also little evidence for present-day extension within the WARS. Overall seismicity is low to non-existent (Winberry & Anandakrishnan 2003; Lough *et al.* 2013), and GPS data resolve little, if any, horizontal strain (Donnellan & Luyendyk 2004; Wilson *et al.* 2014).

MBLD consists mainly of a low-relief dome capped by several Cenozoic volcanoes (Mukasa & Dalziel 2000). Although the most common rock type exposed is alkaline basalt, the basalts are covered in many places by felsic lavas forming N–S and E–W oriented volcanic chains (LeMasurier & Rex 1989). A suite of mafic dykes across the MBLD was used by Storey *et al.* (1999) to infer that a mid-Cretaceous mantle plume could still be situated underneath MBLD today. Recent body and surface wave tomography images show an upper-mantle low-velocity structure beneath MBLD, consistent with a mantle plume interpretation (Hansen *et al.* 2014; Lloyd *et al.* 2015; Heeszel *et al.* 2016), and mantle transition zone thinning imaged beneath the Ruppert Coast of Marie Byrd Land suggests a possible lower-mantle plume source (Emry *et al.* 2015).

### 2.2 East Antarctica

Because a thick ice sheet covers most of EA, its geologic composition and tectonic history remain enigmatic (Adie 1962; Dalziel 1992). Most of EA is thought to be a large and stable Precambrian craton, comprised of Proterozoic and Archean terrains (Moores 1991; Dalziel 1992; Fitzsimons 2000). The physiographic regions of EA relevant to this study are the Gamburtsev Mountains (GAM), the Vostok Highlands (VHIG), and the Wilkes Basin (WILK) (Fig. 1).

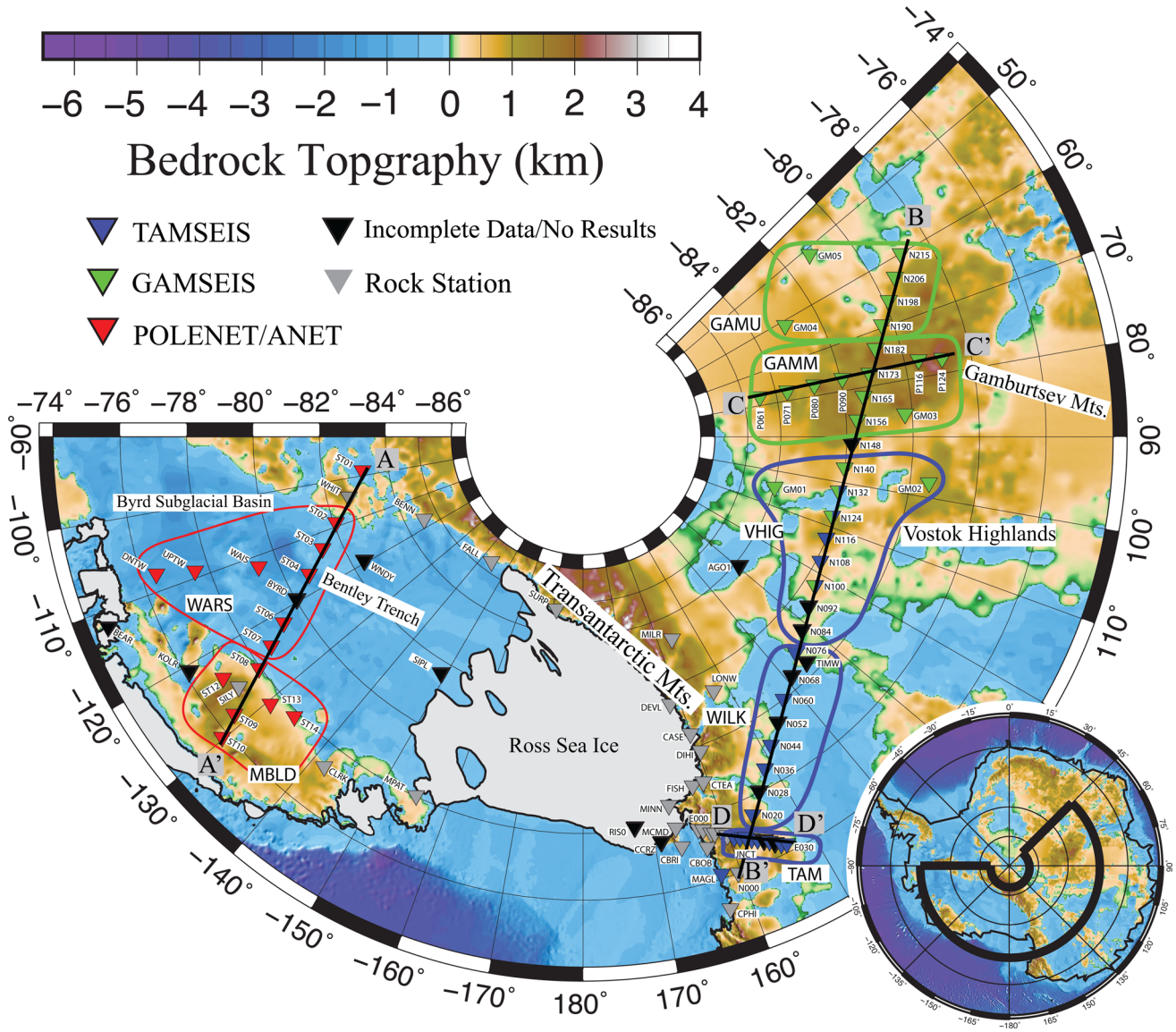


**Figure 1.** Location of seismic stations used in this study and bedrock elevations from BEDMAP2 (Fretwell *et al.* 2013). The coloured lines show the grouping of stations explained in the text. Upper Gamburtsev Mountains (GAMU), Middle Gamburtsev Mountains (GAMM), Vostok Highlands (VHIG), Transantarctic Mountains (TAM), West Antarctic Rift System (WARS) and Marie Byrd Land Dome (MBLD). Thin black lines show the location of the cross-sections A–A′, B–B′, C–C′ and D–D′ in Fig. 5.

The GAM, situated near the centre of EA, have high and relatively fresh alpine topography (Ferraccioli *et al.* 2011) and are supported by a thick crustal root (Hansen *et al.* 2010). We separate the GAM into upper (GAMU) and middle (GAMM) sections based on subglacial topography to facilitate discussion of the results (Fig. 1). The WILK is a 1250 km long, 100–400 km wide subglacial feature (Drewry 1976) located adjacent and subparallel to the TAM. The VHIG encompass the region between the GAM and the WILK.

### 2.3 Transantarctic Mountains

The TAM are ∼200 km wide, ∼4 km high and extend ∼4000 km across the interior of Antarctica, forming a boundary between EA and WA. Uplift of the mountains, constrained by apatite fission track analysis, began in the early Cenozoic (Fitzgerald 1992). Basement rocks in the TAM consist mainly of Precambrian and Cambrian meta-sediments and Cambro-Ordovician granites, unconformably overlain by the Beacon supergroup (Fitzgerald 1992). Lacking any evidence for a compressional origin, the TAM are the largest non-collisional mountain range in the world, and their origin remains widely debated (e.g. Fitzgerald *et al.* 1986; Stern & ten Brink 1989; ten Brink *et al.* 1997; Studinger *et al.* 2004; Huerta & Harry 2007).

## 3 DATA

This study utilizes data from three different experiments that include numerous broad-band seismic stations that have been deployed on ice across Antarctica (Fig. 1). The Transantarctic Mountains Seismic Experiment (TAMSEIS) consisted of 42 seismic stations deployed between 2000 and 2003 in three arrays: (1) a 16 station east–west oriented array with ∼20 km interstation spacing, including 10 ice stations (E012-E030), (2) a 17 station north–south oriented array with ∼80 km interstation spacing, with all stations deployed on ice (N000-N132) and (3) a nine station array deployed on rock

spread along the coastal area near Ross Island (Lawrence *et al.* 2006; Watson *et al.* 2006). The Gamburtsev Mountains Seismic Experiment (GAMSEIS) consisted of 26 stations deployed on ice (Lloyd *et al.* 2013). Twelve stations were installed to extend the north–south TAMSEIS array, with two reoccupied stations (N124 and N132). A subparallel array was also deployed south of the north–south transect, which included seven stations, and another six stations were installed that formed a crossing transect to improve 2D data coverage (Fig. 1). We also use data from POLENET-ANET (WA and TAM portions of the Polar Earth Observing Network; Fig. 1). This deployment consisted of 16 rock stations and 19 ice stations, including a backbone array that was deployed between 2008 and 2012 and a temporary transect that was deployed between 2010 and 2012 (Chaput *et al.* 2014). All POLENET-ANET ice station data that became available after the 2013–2014 field season have been used in this study. For all three experiments (TAMSEIS, GAMSEIS and POLENET), the stations were equipped with broad-band seismometers, and data were recorded at 40 samples per second.

## 4 METHODOLOGY

### 4.1 Receiver function computation

SRFs were generated using the method outlined by Hansen *et al.* 2009a, 2010), with broad-band data from earthquakes with magnitudes $>5.5$ $M_w$, distances between 60° and 80°, and focal depths $<200$ km. This limited range of events eliminates many of the phases that could interfere with the Sp Moho converted phase, as described by Wilson *et al.* (2006). The seismograms were visually inspected to select events with relatively high signal-to-noise ratios and clear *S*-wave arrivals. The traces were rotated from the north–east-vertical coordinate system to the radial–transverse-vertical coordinate system and were cut into segments extending from 100 s prior to the *S*-phase arrival to 12 s after. The receiver functions were computed by deconvolving the radial component from the vertical using the iterative time domain method described by Ligorría & Ammon (1999), and the time and amplitude of the SRFs were reversed to make them visually comparable to PRFs. Receiver functions with high noise levels were removed from the data set, and the remaining receiver functions at each station were stacked. We used a stacking procedure that utilizes the bootstrapping method described in Efron & Tibshirani (1991) to compute error bounds. Receiver functions in each stack were randomly resampled 200 times to obtain 95 per cent error bounds, which are shown on the SRF stacks (Fig. 2).

New data were available for five GAMSEIS stations (GM02, GM05, N140, N215 and P061) compared to the previous analysis of these stations by Hansen *et al.* (2010). For these stations, we used the same events as Hansen *et al.* (2010) but added between 4 and 37 new events per station. For the GAMSEIS and TAMSEIS stations where no new data were available, we used the same events as Hansen *et al.* (2009a, 2010) and recomputed the stacks to obtain bootstrap error bounds. SRFs have not been previously reported for the POLENET stations.

### 4.2 Grid search for crustal structure

Also following the procedure described by Hansen *et al.* (2009a, 2010), a two-step grid search approach was used to estimate the crustal thickness and average crustal shear wave velocity beneath each station. In the first step, we generated 4-layer models to represent the ice, the upper and lower crust and the mantle. The thickness of the ice layer was taken from BEDMAP2 (Fretwell *et al.* 2013), and the *S*-wave velocity of the ice was fixed at 1.9 km $s^{-1}$ (Kohnen 1974). Crustal thickness was varied from 10 to 70 km, with a 1 km increment, and the average crustal shear wave velocity was varied from 3.4 to 3.9 km $s^{-1}$, with a 0.1 km $s^{-1}$ increment. The models were constrained so that velocities in the upper crustal layer had to be equal to or less than the lower layer. Given that mantle velocities in EA are higher than in WA (e.g. Danesi & Morelli 2001; Ritzwoller *et al.* 2001; Lloyd *et al.* 2013; Lloyd *et al.* 2015), the mantle was modelled as a half-space with a fixed *S*-wave velocity of 4.5 km $s^{-1}$ for EA and the TAM, and 4.3 km $s^{-1}$ for WA. The density for each layer was calculated using an empirical *S*-wave velocity versus density relationship from Brocher (2005), and the *P*-wave velocity was calculated using the *S*-wave velocity and a corresponding Poisson's ratio (0.33 for the ice layer, 0.25 for the crust and 0.28 for the mantle). A summary of these values can be found in Table 1.

Each model was used to compute Rayleigh wave phase velocities for periods between 18 and 30 s, and the modelled dispersion curves were then compared to Rayleigh wave phase velocities from Heeszel *et al.* (2016), which were smoothed using a three-point moving average. However, even after applying the three-point moving average, some dispersion curves still exhibited unrealistic changes in phase velocity over a small period range. Within each tectonic region (Fig. 1), the individual dispersion curves were similar, and therefore to further smooth the phase velocity curves used in the grid search, we computed an average dispersion curve for each region (Fig. 1). The maximum deviation between phase velocities in the unsmoothed, individual dispersion curves for each region and the corresponding regional phase velocity average was $\leq 0.08$ km $s^{-1}$. Thus, for the grid search, we used an error bound of $\pm 0.08$ km $s^{-1}$ for the phase velocity at each period, with the phase velocity taken from the average dispersion curve for the region.

Models that yielded synthetic dispersion data within error of the observed phase velocities were then used in the second step of the grid search, in which predicted Moho Sp times for the models were compared to the observed times in the SRF stacks. The corresponding uncertainty used to fit the conversion timing is provided by the bootstrapped error bounds on the SRF stacks. Only models that fit both the observed dispersion data and the observed Moho Sp time within error were considered to be successful. Examples for two stations, one with thick crust (P124) and the other with thin crust (ST03), are shown in Fig. 2.

## 5 RESULTS

### 5.1 Crustal structure

Crustal thickness estimates across Antarctica, which range from 19 to 59 km, are summarized in Fig. 3 and Table 2, and individual station results are provided in the Supporting Information. Histograms are used to show the distribution of the models that fit both the dispersion curves and the Moho Sp arrival time within the prescribed error, and the standard deviation of these models provides an estimate of crustal parameter uncertainty for each station (Fig. 2). However, this estimation does not include uncertainties that arise from the fixed ice thickness, ice shear-wave velocity, or crustal density used in the grid search. As described by Hansen *et al.* (2009a), uncertainties associated with these parameters factor into the overall uncertainty of the crustal structure estimates, averaging 1.5 km for crustal thickness and 0.04 km $s^{-1}$ for average crustal shear wave

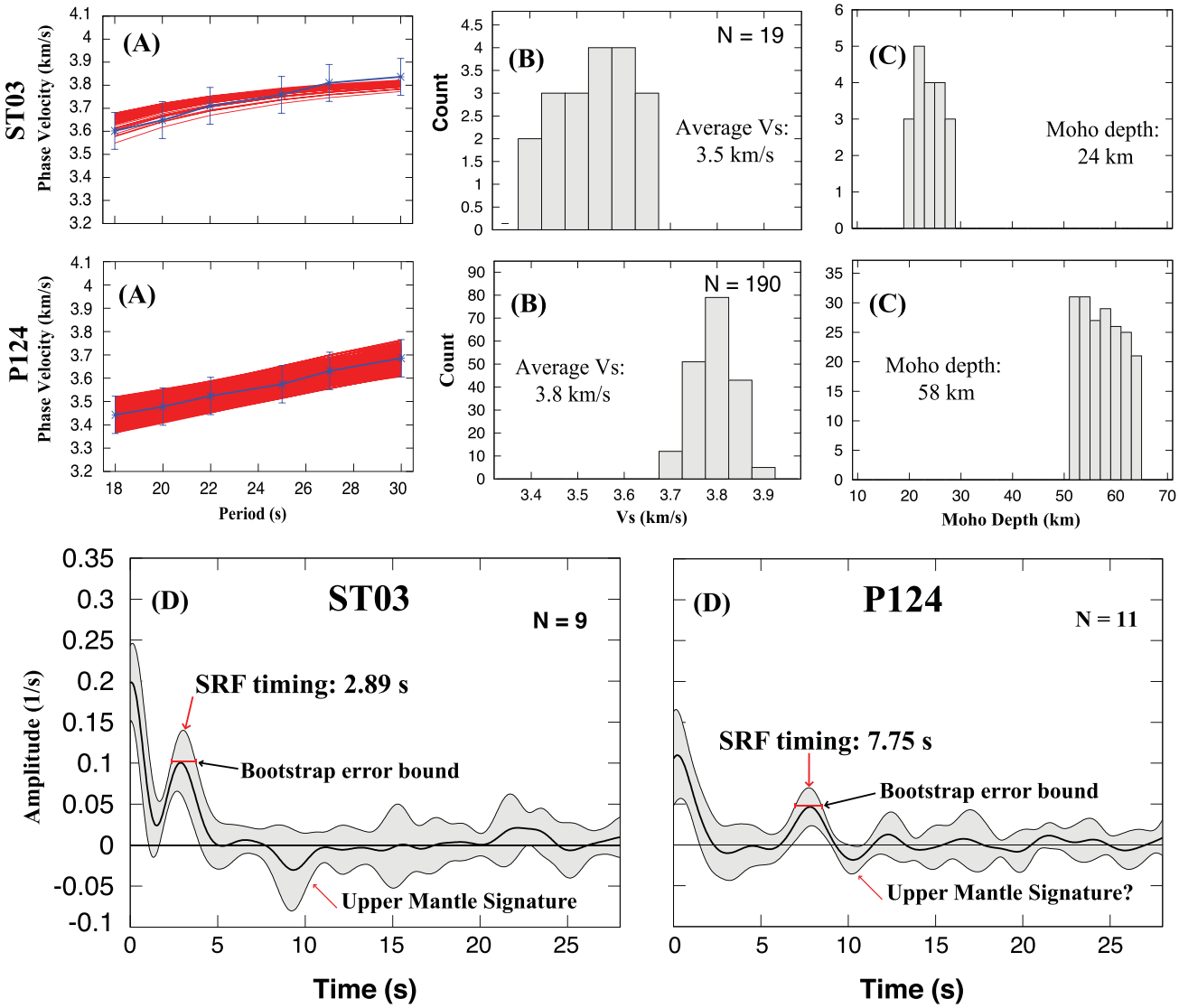


**Figure 2.** Data and modelling results for two stations, ST03 and P124. Panels 'A' show the phase velocity dispersion curves for all models (red lines) that fit the dispersion data provided by Heeszel *et al.* (2016; blue lines with error bars). Panels B and C show the distribution of the average crustal shear velocities and Moho depths for models that fit the dispersion data and Moho Sp timing in the SRF stacks. *N* denotes the total number of models. Panels D show the SRF stack, where the black line is the mean of the stack and the grey shaded areas show the bootstrap error bounds. *N* denotes the number of individual SRFs contributing to each stack.

**Table 1.** Parameters used in the grid search.

| | Thickness (km) | Vp (km $s^{-1}$) | Vs (km $s^{-1}$) | Density (g $cm^{-3}$) | Poisson's ratio (v) |
|---|---|---|---|---|---|
| Ice | BedMap2 | | 1.9 | | 0.33 |
| Upper crust | 10–70 | $Vs\sqrt{\frac{2(v-1)}{2v-1}}$ | 3.4–3.9 | $0.32 \times Vs + 0.77$ | 0.25 |
| Lower crust | 10–70 | | 3.4–3.9 | | 0.25 |
| Mantle | Half-space | | 4.3 or 4.5 | | 0.28 |

velocity. By combining these estimates with the standard deviation of the accepted models, the errors in crustal thickness can, at most stations, be estimated to within 3 km and the mean crustal velocity to within 0.1 km $s^{-1}$. However, for some stations, the standard deviation of the accepted models is greater than 3 km (Fig. 3 and Supporting Information). We chose the larger of the two numbers in every case as our final estimated error for each station (Table 2).

To facilitate a comparison of results, we grouped stations by physiographic region, as shown in Figs 1 and 3. The first region, GAMU, is located just grid north of the GAM, where the average crustal thickness is 49 km and the average crustal *S*-wave velocity is 3.8 km $s^{-1}$. In the central portion of the GAM (GAMM), the average crustal thickness is 54 km, with an average velocity of 3.8 km $s^{-1}$. Moving grid south, the VHIG region has an average crustal thickness of 44 km and velocity of 3.7 km $s^{-1}$, while the WILK has an average crustal thickness of 45 km and a velocity of 3.8 km $s^{-1}$. In the TAM, at roughly −77°S, stations in the east–west TAMSEIS transect are underlain by crust with an average thickness

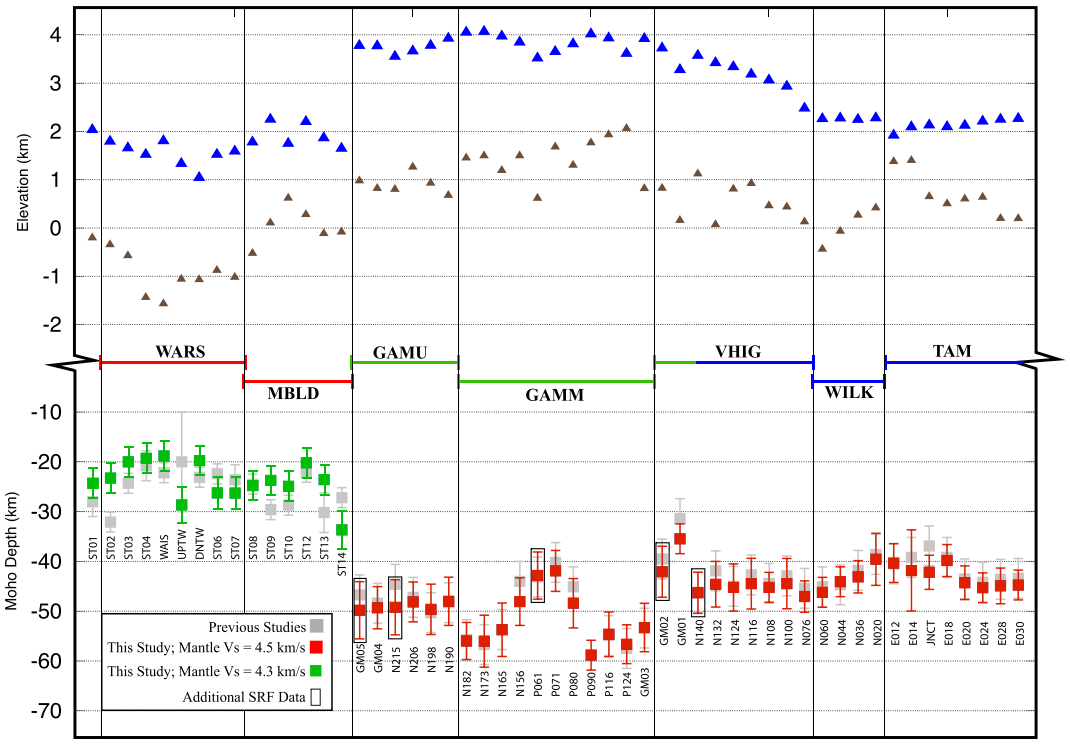


**Figure 3.** Summary of results. Green squares show the crustal thickness results for stations in West Antarctica and red squares are the results for East Antarctica. Grey squares represent previous studies from Hansen *et al.* 2009a, 2010) in East Antarctica and from Chaput *et al.* (2014) in West Antarctica. The brown and blue triangles denote bedrock and ice elevation, respectively. Stations in East Antarctica highlighted with black rectangles are stations where additional seismic data was used for computing SRF stacks compared to Hansen *et al.* (2010). Acronyms of the regions are explained in Fig. 1.

of 43 km and a mean shear velocity of 3.8 km $s^{-1}$. The WARS region displays much thinner crust, averaging 23 km, with an average *S*-wave velocity of 3.6 km $s^{-1}$. Grid south of the WARS, the MBLD displays average crustal thickness of 25 km and an average shear wave velocity of 3.6 km $s^{-1}$.

### 5.2 Upper-mantle structure

Inspection of the SRF stacks shows that roughly half of the stations display a trough, labelled in Fig. 2, within the time window where an Sp conversion from an upper-mantle discontinuity, such as the LAB, would be expected (i.e. ∼1–10 s after the Moho Sp arrival). However, only a few individual stations display such an Sp signal with an amplitude rising above the bootstrapped error bounds, and so the individual station stacks cannot be confidently interpreted (see Supporting Information for individual stations).

In an attempt to improve the associated signal-to-noise ratio, we stacked the individual receiver functions within each physiographic region (Fig. 1). All regional stacks show an Sp arrival from the Moho (Fig. 4). However, the regional stacks from EA and the TAM show little to no indication of an Sp arrival from the LAB, indicating that the LAB may be a gradational boundary beneath these areas. The stacks for the WARS and MBLD stations in WA have a relatively long wavelength (∼10 s), low amplitude negative arrival between ∼5 and 15 s, suggesting that some Sp energy may be arriving from the LAB; however, similar to most of the stacks for individual stations, the signal amplitude does not rise above the bootstrapped error bounds and thus we also do not have confidence in interpreting the WARS and MBLD stacks.

## 6 DISCUSSION

In summary, Sp arrivals from the Moho are evident on the SRF stacks for most stations, and by combining Rayleigh wave phase velocity measurements with the arrival times of the Moho Sp phase, we have been able to estimate Moho depths and mean crustal shear velocities. In contrast, the SRF stacks provide little interpretable information about upper-mantle structure. We therefore focus the discussion on a comparison of our results to those from previous studies of crustal structure, and then use our results to comment on heat flow in EA and WA.

### 6.1 Crustal structure in West Antarctica

Profile B–B′ in Fig. 5 shows a cross-section across WA, extending roughly from Mt. Whitmore to MBLD. The deepest Moho depths are observed under Mt. Whitmore and Mt. Sidley (PRF estimates from Chaput *et al.* 2014), while the shallowest Moho is observed under stations WAIS and ST04 (19 km depth) in the Bentley Subglacial Trench. The crustal thicknesses for stations away from the Bentley Trench range from 20 to 26 km. These results are similar to previously published PRF results from Chaput *et al.* (2014), except for three stations where the results do not fall within the reported uncertainties (Fig. 3). Our results for stations ST09 and ST14 differ by 6 km from Chaput *et al.* (2014), and for station ST02, the difference is 9 km. SRF stacks for these stations show a clear Moho Sp arrival, and the associated error bounds are comparable to those for other stations (see the Supporting Information). Therefore, it is not apparent why there is a notable difference in our Moho depth estimates for these stations compared to Chaput *et al.* (2014).

**Table 2.** Summary of results obtained in this study.

| Station | Latitude | Longitude | Crustal thickness (km) | Vs (km $s^{-1}$) | Elevation (km) | Ice thickness (km) |
|---|---|---|---|---|---|---|
| E012 | −77.05 | 159.32 | 41 ± 4 | 3.7 | 1.92 | 0.24 |
| E014 | −76.99 | 158.62 | 43 ± 8 | 3.7 | 2.09 | 0.69 |
| E018 | −76.82 | 157.22 | 40 ± 3 | 3.7 | 2.09 | 1.90 |
| E020 | −76.73 | 156.54 | 44 ± 3 | 3.8 | 2.12 | 1.63 |
| E024 | −76.54 | 155.23 | 45 ± 3 | 3.8 | 2.21 | 1.51 |
| E028 | −76.31 | 154.04 | 45 ± 4 | 3.8 | 2.25 | 1.65 |
| E030 | −76.25 | 153.38 | 45 ± 3 | 3.8 | 2.26 | 1.79 |
| JNCT | −76.93 | 157.90 | 42 ± 3 | 3.8 | 2.13 | 1.48 |
| N020 | −77.47 | 155.89 | 40 ± 5 | 3.7 | 2.28 | 1.52 |
| N036 | −78.55 | 151.29 | 42 ± 3 | 3.7 | 2.24 | 2.58 |
| N044 | −79.07 | 148.62 | 44 ± 3 | 3.7 | 2.27 | 2.34 |
| N060 | −80.00 | 142.60 | 46 ± 3 | 3.8 | 2.26 | 2.80 |
| N076 | −80.81 | 135.43 | 47 ± 3 | 3.8 | 2.48 | 2.59 |
| N100 | −81.65 | 122.61 | 44 ± 5 | 3.7 | 2.93 | 2.56 |
| N108 | −81.88 | 117.61 | 45 ± 3 | 3.8 | 3.06 | 2.66 |
| N116 | −82.01 | 112.57 | 44 ± 5 | 3.7 | 3.18 | 2.33 |
| N124 | −82.07 | 107.64 | 45 ± 5 | 3.8 | 3.33 | 2.50 |
| N132 | −82.06 | 101.96 | 44 ± 5 | 3.8 | 3.42 | 3.55 |
| N140 | −82.01 | 96.77 | 46 ± 4 | 3.8 | 3.57 | 3.03 |
| N156 | −81.67 | 86.50 | 48 ± 5 | 3.7 | 3.84 | 2.84 |
| N165 | −81.41 | 81.76 | 54 ± 5 | 3.8 | 3.97 | 2.47 |
| N173 | −81.11 | 77.47 | 56 ± 5 | 3.8 | 4.07 | 2.74 |
| N182 | −80.74 | 73.19 | 56 ± 4 | 3.8 | 4.05 | 2.64 |
| N190 | −80.33 | 69.43 | 48 ± 5 | 3.8 | 3.92 | 3.09 |
| N198 | −79.86 | 65.96 | 49 ± 5 | 3.8 | 3.78 | 3.06 |
| N206 | −79.40 | 62.86 | 48 ± 4 | 3.8 | 3.66 | 2.96 |
| N215 | −78.91 | 59.99 | 49 ± 6 | 3.8 | 3.55 | 3.07 |
| GM01 | −83.99 | 104.73 | 35 ± 3 | 3.6 | 3.27 | 3.30 |
| GM02 | −79.43 | 97.58 | 42 ± 5 | 3.7 | 3.72 | 2.74 |
| GM03 | −80.22 | 85.94 | 54 ± 5 | 3.8 | 3.92 | 2.33 |
| GM04 | −83.00 | 61.11 | 49 ± 4 | 3.8 | 3.77 | 3.00 |
| GM05 | −81.18 | 51.16 | 49 ± 6 | 3.8 | 3.77 | 3.53 |
| P061 | −84.50 | 77.22 | 43 ± 5 | 3.7 | 2.51 | 2.96 |
| P071 | −83.65 | 77.33 | 42 ± 4 | 3.7 | 3.65 | 2.18 |
| P080 | −82.81 | 77.36 | 49 ± 5 | 3.7 | 3.81 | 1.77 |
| P090 | −81.94 | 77.31 | 59 ± 3 | 3.8 | 4.01 | 2.25 |
| P116 | −79.57 | 77.06 | 55 ± 4 | 3.8 | 3.93 | 1.75 |
| P124 | −78.87 | 77.66 | 57 ± 4 | 3.8 | 3.61 | 1.65 |
| ST01 | −83.23 | −98.74 | 24 ± 3 | 3.5 | 2.03 | 2.24 |
| ST02 | −82.07 | −109.13 | 23 ± 3 | 3.6 | 1.79 | 2.14 |
| ST03 | −81.41 | −113.15 | 20 ± 3 | 3.5 | 1.66 | 2.23 |
| ST04 | −80.72 | −116.58 | 19 ± 3 | 3.5 | 1.52 | 2.96 |
| ST06 | −79.33 | −121.82 | 26 ± 3 | 3.7 | 1.52 | 2.40 |
| ST07 | −78.64 | −123.79 | 26 ± 3 | 3.7 | 1.59 | 2.61 |
| ST08 | −77.95 | −125.53 | 25 ± 3 | 3.6 | 1.78 | 2.30 |
| ST09 | −76.53 | −128.47 | 24 ± 3 | 3.6 | 2.25 | 2.14 |
| ST10 | −75.81 | −129.75 | 25 ± 3 | 3.6 | 1.75 | 1.13 |
| ST12 | −76.90 | −123.82 | 20 ± 3 | 3.5 | 2.20 | 1.92 |
| ST13 | −77.56 | −130.51 | 24 ± 3 | 3.6 | 1.86 | 1.98 |
| ST14 | −77.84 | −134.08 | 34 ± 4 | 3.7 | 1.64 | 1.73 |
| UPTW | −77.58 | −109.04 | 29 ± 4 | 3.7 | 1.33 | 2.39 |
| DNTW | −76.46 | −107.78 | 20 ± 3 | 3.5 | 1.03 | 2.11 |
| WAIS | −79.42 | −111.78 | 19 ± 3 | 3.5 | 1.80 | 3.37 |

Other previous seismic studies of crustal thickness in the WARS have been more localized or else have focused on the Ross Sea region in WA. Winberry & Anandakrishnan (2004) found crustal thicknesses of 21–31 km beneath the WARS, with the thinnest crust (21 km) under the Bentley Trench, comparable to our findings. Trey *et al.* (1999) reported crustal thinning from ∼24 to ∼14 km under the Central Trough and the Eastern Basin in the western WARS. While the spatial resolution of the Trey *et al.* (1999) study is better than in our cross-section (Fig. 5), the horizontal scale over which the crustal thinning is observed, on the order of 100 km, as well as the total amount of crustal thinning (∼10 km) is similar to what we find for the Bentley Trench. The crustal shear velocity model from Trey *et al.* (1999) shows velocities ranging from 3.0 to 3.6 km $s^{-1}$ in the upper crust and 3.6 to 4.1 km $s^{-1}$ in the lower crust, comparable to the average crustal shear velocities ranging from 3.5 to 3.7 km $s^{-1}$ for stations ST02–ST08. The similarities in both crustal thickness and shear velocity structure between the Ross Sea sector of the WARS and eastern WARS suggest that first-order basin

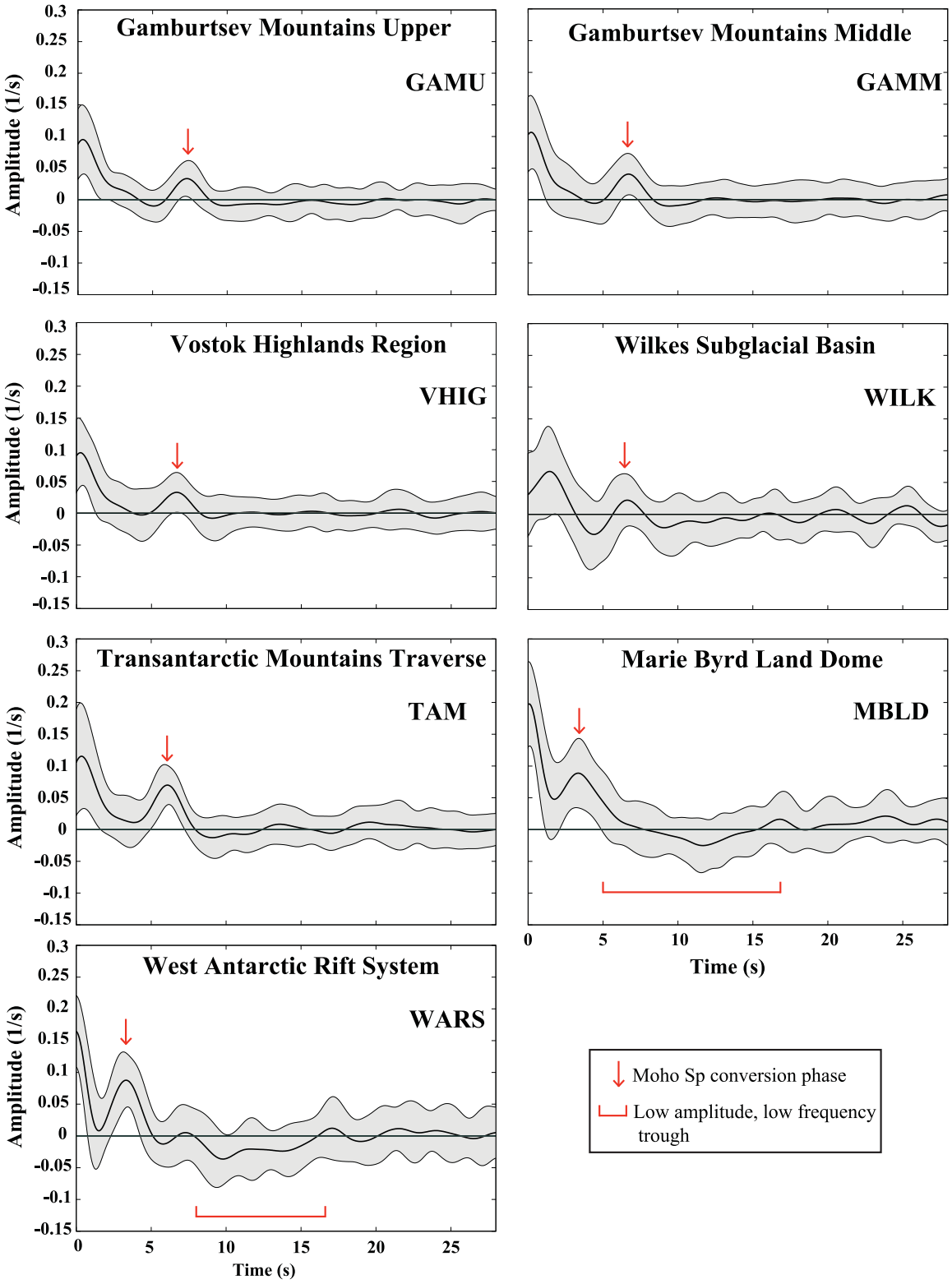


**Figure 4.** Regional SRF stacks. The black lines denote the mean of the stacks and the grey shaded areas are the bootstrap error bounds. The Moho Ps phase is clearly observed in all panels. WARS and MBLD SRF stacks show energy arriving in the 5–15 s window that may be coming from upper-mantle discontinuities.

structures could be related and/or were created by similar processes. Our findings are also broadly consistent with gravity-derived crustal thickness estimates from O'Donnell & Nyblade (2014), differing by an average of only ∼5 km. These differences are most prominent within MBLD and the Bentley Trench.

### 6.2 Crustal structure in East Antarctica

Profiles A–A′ and C–C′ in Fig. 5 show thick crust beneath the GAMU and GAMM regions. Stations N215–N190 are underlain by 47–49 km thick crust that increases to 54–56 km beneath stations

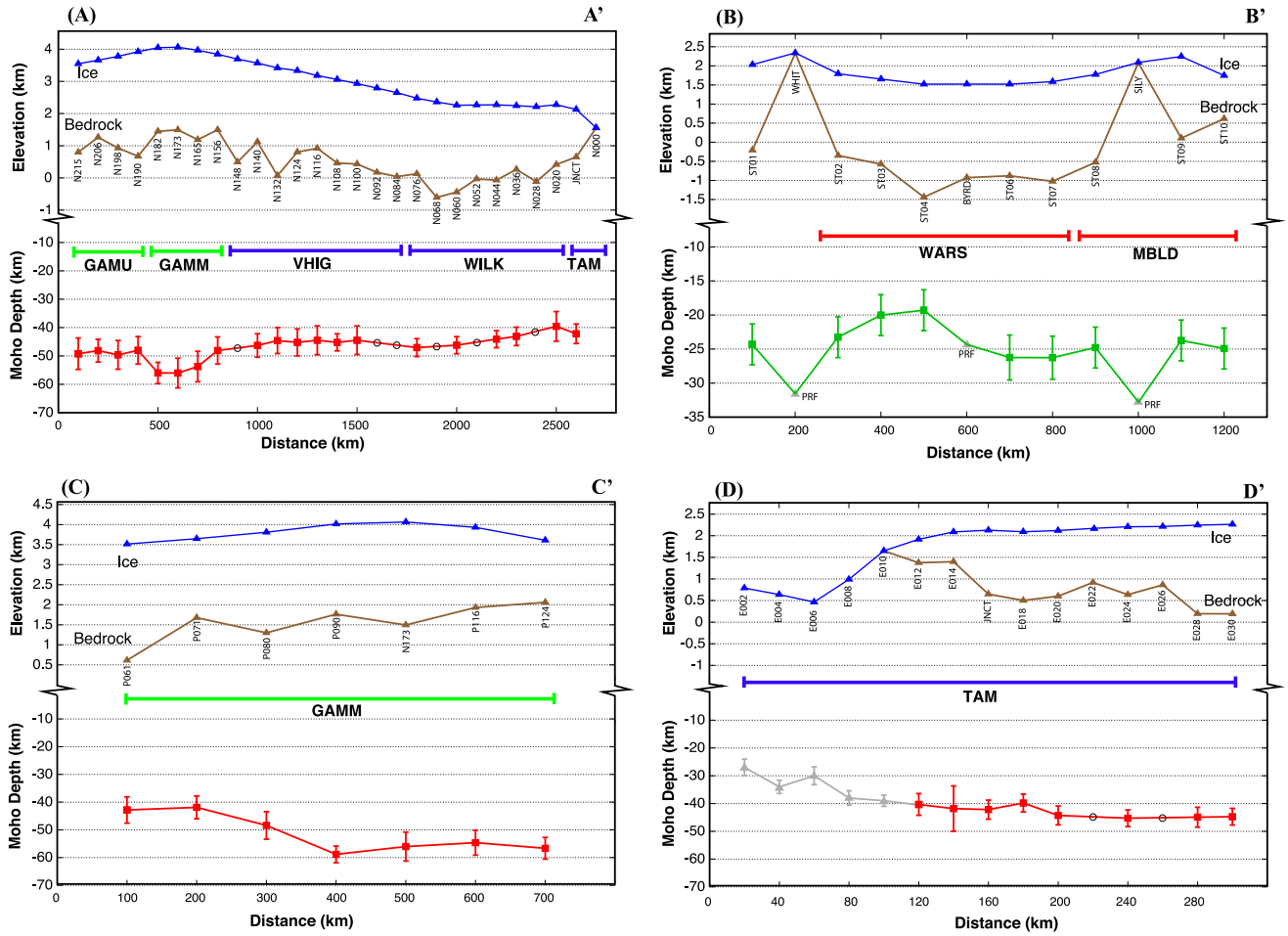


**Figure 5.** Cross-section profiles showing ice surface elevations, bedrock elevations and Moho depths. Labels are the same as in Fig. 3. The locations of the cross-sections are shown in Fig. 1. Grey symbols give Moho depths at rock stations determined from *P*-wave receiver functions (Finotello *et al.* 2011; Chaput *et al.* 2014). Open circles are shown on the profiles for stations where no SRF Moho depth determinations were obtained (same stations as indicated in Fig. 3).

N182–N165. The thickest crust is also coincident with the highest bedrock elevations in the GAM. The VHIG are underlain by uniformly thick crust (45–47 km), but the crust under the WILK thins from 46 km beneath station N076 to 40 km beneath station N020. Stations across the TAM (Fig. 5, profile D–D′) display crustal thicknesses of 40–42 km, while stations grid east of station E018 display somewhat thicker crust (44–45 km).

All of the crustal thickness estimates from the GAMU, GAMM, VHIG, WILK and TAM regions match previous results from Hansen *et al.* (2009a, 2010) within reported uncertainty estimates (Fig. 3). Differences of a few kilometres in crustal thickness for some stations can be attributed to the different error bounds used for the Moho Sp arrival time, differences in Rayleigh wave phase velocities and, in some cases, the addition of new data, which yielded slightly different Moho Sp times. The results presented here are also in agreement with gravity-derived crustal thickness estimates from O'Donnell & Nyblade (2014). On average, our results in EA differ from their estimates by less than 4 km.

### 6.3 Implications for heat flow

Geothermal heat flux is an important factor that can greatly influence the stability of ice sheets (e.g. Huybrechts *et al.* 1993; Parizek 2002; Bennett 2003; Pollard *et al.* 2005; Pollard & DeConto 2009; Pattyn 2010), and the WAIS in particular may be susceptible to collapse in part because of possibly elevated heat flow in WA (Blankenship *et al.* 1993; Schroeder *et al.* 2014; Fisher *et al.* 2015). There are only a few measurements of heat flow from the continent. Clow *et al.* (2012) reported a single measurement of 240 mW $m^{-2}$ from a deep ice core site in the middle of the WAIS. Borehole measurements from Siple Dome yielded a heat flow of 69 mW $m^{-2}$ (Engelhardt 2004), Morin *et al.* (2010) reported a heat flow of 115 mW $m^{-2}$ from a borehole located on the McMurdo Ice Shelf, and Fisher *et al.* (2015) recently reported a heat flow of 285 mW $m^{-2}$ below subglacial Lake Whillhans.

Proxy methods have also been used to estimate heat flow in Antarctica. From modelling magnetic data, Fox-Maule *et al.* (2005) suggested that heat flow in EA is ∼50 to 60 mW $m^{-2}$ and ∼55 to 65 mW $m^{-2}$ in WA, with slightly higher heat flow near areas with Cenozoic-recent volcanoes and the Siple coast. Pollard *et al.* (2005) estimated heat flow using global average values for similar aged terrains as those found in Antarctica. In their heat flow map, estimates ranged from 40 to 55 mW $m^{-2}$ in EA and 60 to 70 mW $m^{-2}$ in WA. Blankenship *et al.* (1993) reported elevated heat flow in WA from interpreting aerogeophysical data, including extremely high heat flow of 10–25 W $m^{-2}$, which they attributed to an isolated volcanic vent. And in another study of WA, Schroeder *et al.* (2014) used airborne radar to infer a high heat flow of ∼114 ± 10 mW $m^{-2}$

for the Thwaites Glacier hydrologic catchment, with heat flow in a few areas exceeding 200 mW $m^{-2}$. They attributed the elevated heat flow to magmatic activity.

To examine the implications of our findings for heat flow across Antarctica, we compare our crustal thickness estimates in three areas of EA and one in WA to estimates from other tectonically similar terrains where heat flow has been measured. A number of authors (e.g. Tessensohn & Woörner 1991; LeMasurier 2008) have suggested as possible analogues to the WARS the East African rift system and the Basin and Range province, which have eleveated heat flow (Morgan 1982), and the Newfoundland–Iberia passive margins and the North Sea rift, which do not have elevated heat flow. The Cenozoic Basin and Range province in North America is associated with thicker crust than the WARS, ranging from ∼28 to ∼35 km (Zandt *et al.* 1995). The Rio Grande rift in central New Mexico, on the eastern edge of the southern Basin and Range, also has thicker crust than the WARS, with an average Moho depth of ∼35 km (Wilson *et al.* 2005). Within the Cenozoic East African rift system, the Kenya rift has Moho depths ranging from ∼25 to 44 km with an average of ∼35 km (Prodehl *et al.* 1997 and references therein), and in the Main Ethiopian Rift, Moho depths range from 26 to 40 km (Maguire *et al.* 2006). Other well-studied Cenozoic rifts with elevated heat flow, such as the Baikal rift and the Rhine Graben (Morgan 1982), also have thicker crust than the WARS (e.g. 38–42 km for the Baikal rift and 30 km for the Rhine Graben; Brun *et al.* 1992; ten Brink & Taylor 2002). Because there are significant differences in crustal thicknesses between these Cenozoic rifts and the WARS, they are probably associated with different extensional processes and histories and therefore may not be good analogues for the WARS.

The Newfoundland–Iberia passive margins formed mainly in the Cretaceous, similar to the WARS. Crustal thicknesses off Newfoundland average ∼25 to ∼30 km, including a 5–6 km thick mafic underplate (Reid 1993, 1994). Dean *et al.* (2000) found ∼28 km thick crust on the conjugate margin offshore Iberia, at the continental-oceanic crust transition. After accounting for the 5–6 km of underplating, the similarities in crustal thickness between the Newfoundland–Iberia margins and the WARS indicate that the crust has been thinned by a comparable amount in both regions, assuming that both regions had typical continental crust that was ∼35–40 km thick prior to rifting.

Given the similarities between the WARS and the Newfoundland–Iberia passive margin, both in terms of the rift timing and the crustal structure, the extensional processes that formed them and their extensional histories may be quite similar. Consequently, heat flow from the Newfoundland–Iberia basins may provide a reasonable proxy for heat flow broadly across the WARS. Heat flow measurements for the Newfoundland and Iberia basins range from 40 to 65 mW $m^{-2}$ (Pollack *et al.* 1993; Fernàndez *et al.* 1998; Davies 2013). These values are not elevated, which indicates that the lithospheric thermal anomaly associated with rifting has dissipated.

A similar conclusion can be reached by comparing the WARS and the North Sea rift, although rifting in the North Sea probably began in the Triassic, somewhat earlier than in the WARS. Nonetheless, the major phase of extension in the North Sea rift occurred in the mid-Jurassic to mid-Cretaceous and crustal thickness, which is ∼20–30 km on average and 15 km at its thinnest (Beach *et al.* 1987; Klemperer 1988), make it a possible analogue for the WARS. Heat flow in the North Sea is between 60 and 85 mW $m^{-2}$, only slightly higher than in the Newfoundland–Iberia passive margins.

Thus, using the Newfoundland–Iberia passive margins and the North Sea rift as tectonic analogues to the WARS, it can be argued that heat flow in the WARS need not be elevated, consistent with the findings of Fox-Maule *et al.* (2005), who reported heat flow for the WARS of ∼55–65 mW $m^{-2}$. This conclusion, however, does not preclude the possibility of elevated heat flow localized within narrow Cenozoic rifts that may have developed subsequently to the broader Cretaceous rift system, or in areas of Cenozoic-recent magmatic activity within the WARS.

In EA, most of the crust is either Proterozoic or Archean in age, as reviewed previously. Precambrian crust typically exhibits Moho depths of ∼35 to 45 km (Christensen & Mooney 1995; Rudnick & Fountain 1995; Zandt & Ammon 1995; Tugume *et al.* 2013; Kachingwe *et al.* 2015). Crustal thicknesses in EA, outside of the GAM, average ∼40 to 45 km, which is consistent with an interpretation of Proterozoic and/or Archean crust beneath the EA ice sheet. Average global heat flow estimates in Proterozoic terrains vary between 46 to 58 mW $m^{-2}$ and in Archean terranes between 41 to 51 mW $m^{-2}$ (Nyblade & Pollack 1993; Pollack *et al.* 1993). Therefore, heat flow across much of EA is likely in the 41–58 mW $m^{-2}$ range. This conclusion is consistent with heat flow estimates from Pollack *et al.* (1993), Fox-Maule *et al.* (2005), Davies (2013), and Pollard *et al.* (2005).

## 7 SUMMARY

Crustal thickness and shear velocity structure across Antarctica have been investigated by modelling SRFs and surface wave measurements for temporary stations deployed on ice. In EA, we find 43–58 km thick crust beneath the GAM, 39–46 km thick crust beneath the WILK, and 36–47 km thick crust beneath the VHIG. In the TAM, crustal thickness varies between 39 and 45 km, and in WA, the WARS crustal thickness varies from 19 to 29 km and 20–35 km beneath the MBLD. SRF stacks for the GAM, VHIG, WILK and TAM show little evidence of Sp arrivals coming from upper-mantle depths. SRF stacks for WARS and MBLD suggest that there is some Sp energy arriving from upper-mantle depths but arrival amplitudes do not rise above the bootstrapped uncertainties, and therefore are not interpreted.

Crustal structure in EA is similar to Precambrian crust elsewhere around the world, where heat flow is low, suggesting that heat flux across much of EA is not elevated. Cenozoic rifts, such as the East Africa rift system and the Basin and Range, have substantially thicker crust than the WARS and may not be good analogues for inferring heat flow in the WARS. In comparison, crustal thicknesses in the WARS are similar to the Cretaceous Newfoundland–Iberia rifted margins and the Mesozoic-Tertiary North Sea rift, perhaps providing better analogues. Heat flow in the Newfoundland–Iberia rifted margins and the North Sea rift is not elevated (40 to 85 mW $m^{-2}$), indicating that rift-related heating of the lithosphere has dissipated. By analogy, heat flow broadly across the WARS need not be elevated. However, this conclusion does not rule out the possibility of high heat flow in WA associated with localized Cenozoic extension and/or Cenozoic-recent magmatic activity.

## ACKNOWLEDGEMENTS

The NSF Office of Polar Programs grants 0632230, 0632239, 0652322, 0632335, 0632136, 0632209 and 0632185 support the POLENET-ANET program. All of the seismic deployments incorporated in this study were made possible by the Incorporated

Research Institutions for Seismology (IRIS) through the PASSCAL Instrument Center at New Mexico Tech. Seismic data are available from the IRIS Data Management Center. The facilities of the IRIS Consortium are supported by the National Science Foundation under Cooperative agreement EAR-1063471. Figures in this study were made using the freely available software packages of 'Octave' and 'Generic Mapping Tools (GMT)'. We would like to thank the seismology research group at The Pennsylvania State University for valuable discussion and improvements in the drafting of this manuscript, and two anonymous reviewers for their helpful comments.

## REFERENCES

Adie, R.J., 1962. The geology of Antarctica, *Tectonophysics,* 6371–6371, doi:10.1306/9780891810650.

Artemieva, I.M. & Mooney, W.D., 2001. Thermal thickness and evolution of Precambrian lithosphere: a global study, *J. geophys. Res.,* **106,** 16 387–16 414.

Beach, A., Bird, T. & Gibbs, A., 1987. Extensional tectonics and crustal structure: deep seismic reflection data from the northern North Sea Viking graben, *Geol. Soc. Lond., Spec. Publ.,* **28,** 467–476.

Behrendt, J.C., 1999. Crustal and lithospheric structure of the west Antarctic Rift System from geophysical investigations - a review, *Glob. Planet. Change,* **23,** 25–44.

Behrendt, J.C., LeMasurier, W.E., Cooper, A.K., Tessensohn, F., Tréhu, A. & Damaske, D., 1991. Geophysical studies of the West Antarctic Rift System, *Tectonics,* **10,** 1257–1273.

Bennett, M.R., 2003. Ice streams as the arteries of an ice sheet: Their mechanics, stability and significance, *Earth-Sci. Rev.,* **61,** 309–339.

Blankenship, D.D., Bell, R.E., Hodge, S.M., Brozena, J.M., Behrendt, J.C. & Finn, C.A., 1993. Active volcanism beneath the West Antarctic Ice Sheet and implications for ice-sheet stability, *Nature,* **361,** 526–529.

Brocher, T.M., 2005. Empirical relations between elastic wavespeeds and density in the Earth's crust, *Bull. seism. Soc. Am.,* **95,** 2081–2092.

Brun, J.P. & Gutscher, M.A. & DEKORP-ECORS teams, 1992. Deep crustal structure of the Rhine Graben from DEKORP-ECORS seismic reflection data: a summary, *Tectonophysics,* **208,** 139–147.

Cande, S.C. & Stock, J.M., 2004. Pacific-Antarctic-Australia motion and the formation of the Macquarie Plate, *Geophys. J. Int.,* **157,** 399–414.

Chaput, J. *et al.*, 2014. The crustal thickness of West Antarctica, *J. geophys. Res.,* **119,** 378–395.

Christensen, N.I. & Mooney, W.D., 1995. Seismic velocity structure and composition of the continental crust: a global view, *J. geophys. Res.,* **100,** 9761–9788.

Clow, G.D., Cuffey, K.M & Waddington, E. D., 2012. High heat-flow beneath the central portion of the West Antarctic Ice Sheet, *American Geophysical Union, Fall Meeting 2012,* abstract #C31A-0577.

Dalziel, I.W.D., 1992. Antarctica; a tale of two supercontinents?, *Annu. Rev. Earth Planet. Sci.,* **20,** 501–526.

Dalziel, I.W.D. & Elliot, D.H., 1982. West Antarctica: problem child of Gondwanaland, *Tectonics,* **1**(1), 3–19.

Danesi, S. & Morelli, A., 2001. Structure of the upper mantle under the Antarctic Plate from surface wave tomography, *Geophys. Res. Lett.,* **28,** 4395–4398.

Davies, J.H., 2013. Global map of solid Earth surface heat flow, *Geochem. Geophys. Geosyst.,* **14,** 4608–4622.

Davies, J.H. & Davies, D.R., 2010. Earth's surface heat flux, *Solid Earth,* **1,** 5–24.

Dean, S.M., Minshull, T.A., Whitmarsh, R.B. & Louden, K.E., 2000. Deep structure of the ocean-continent transition in the southern Iberia Abyssal Plain from seismic refraction profiles: the IAM-9 transect at 40°20′N, *J. geophys. Res.,* **105,** 5859–5885.

Donnellan, A. & Luyendyk, B. P., 2004. GPS evidence for a coherent Antarctic plate and for postglacial rebound in Marie Byrd Land, *Glob. planet. Change,* **42**(1), 305–311.

Drewry, D.J., 1976. Sedimentary basins of the east antarctic craton from geophysical evidence, *Tectonophysics,* **36,** 301–314.

Efron, B. & Tibshirani, R., 1991. Statistical data analysis in the computer age, *Science,* **253**(5018), 390–395.

Emry, E.L., Nyblade, A., Julia, J., Anandakrishnan, S., Aster, R.C., Wiens, D., Huerta, A.D. & Wilson, T.J., 2015. The mantle transition zone beneath West Antarctica: seismic evidence for hydration and thermal upwellings, *Geochem. Geophys. Geosyst.,* **16,** 40–58.

Engelhardt, H., 2004. Ice temperature and high geothermal flux at Siple Dome, West Antarctica, from borehole measurements, *J. Glaciol.,* **50,** 251–256.

Fernàndez, M., Marzán, I., Correia, A. & Ramalho, E., 1998. Heat flow, heat production, and lithospheric thermal regime in the Iberian Peninsula, *Tectonophysics,* **291,** 29–53.

Ferraccioli, F., Finn, C.A., Jordan, T., Bell, R.E., Anderson, L. & Damaske, S., 2011. East Antarctic rifting triggers uplift of the Gamburtsev Mountains, *Nature,* **479,** 388–392.

Fielding, C.R., Whittaker, J., Henrys, S.A., Wilson, T.J. & Naish, T.R., 2008. Seismic facies and stratigraphy of the Cenozoic succession in McMurdo Sound, Antarctica: Implications for tectonic, climatic and glacial history, *Palaeogeogr. Palaeoclimatol. Palaeoecol.,* **260,** 8–29.

Finotello, M., Nyblade, A., Julia, J., Wiens, D. & Anandakrishnan, S., 2011. Crustal Vp-Vs ratios and thickness for Ross Island and the Transantarctic Mountain front, Antarctica, *Geophys. J. Int.,* **185,** 85–92.

Fisher, A.T., Mankoff, K.D., Tulaczyk, S.M. & Tyler, S.W., 2015. High geothermal heat flux measured below the West Antarctic Ice Sheet, *Geophysics,* **1,** 1–9.

Fitzgerald, P.G., 1992. The transantarctic mountains of Southern Victoria Land: the Application of apatite fission track analysis to a Rift Shoulder uplift, *Tectonophysics,* **11,** 634–662.

Fitzgerald, P.G., Sandiford, M., Barrett, P.J. & Gleadow, A.J.W., 1986. Asymmetric extension associated with uplift and subsidence in the Transantarctic Mountains and Ross Embayment, *Earth planet. Sci. Lett.,* **81,** 67–78.

Fitzsimons, I.C.W., 2000. A review of tectonic events in the East Antarctic Shield and their implications for Gondwana and earlier supercontinents, *J. Afr. Earth Sci.,* **31,** 3–23.

Ford, H.A., Fischer, K.M., Abt, D.L., Rychert, C.A. & Elkins-Tanton, L.T., 2010. The lithosphere-asthenosphere boundary and cratonic lithospheric layering beneath Australia from Sp wave imaging, *Earth planet. Sci. Lett.,* **300,** 299–310.

Fox-Maule, C., Purucker, M.E., Olsen, N. & Mosegaard, K., 2005. Heat flux anomalies in Antarctica revealed by satellite magnetic data, *Science,* **309,** 464–467.

Fretwell, P. *et al.*, 2013. Bedmap2: Improved ice bed, surface and thickness datasets for Antarctica, *Cryosphere,* **7,** 375–393.

Granot, R., Cande, S.C., Stock, J.M., Davey, F.J. & Clayton, R.W., 2010. Postspreading rifting in the Adare Basin, Antarctica: regional tectonic consequences, *Geochem. Geophys. Geosyst.,* **11,** 1–29.

Hansen, S.E., Julià, J., Nyblade, A.A., Pyle, M.L., Wiens, D. & Anandakrishnan, S., 2009a. Using *S* wave receiver functions to estimate crustal structure beneath ice sheets: an application to the Transantarctic Mountains and East Antarctic craton, *Geochem. Geophys. Geosyst.,* **10,** doi:10.1029/2009GC002576.

Hansen, S.E., Nyblade, A.A., Julià, J. & Dirks, P.H.G.M. Durrheim, R.J., 2009b. Upper-mantle low-velocity zone structure beneath the Kaapvaal craton from *S*-wave receiver functions, *Geophys. J. Int.,* **178,** 1021–1027.

Hansen, S.E., Nyblade, A.A., Heeszel, D.S., Wiens, D.A., Shore, P. & Kanao, M., 2010. Crustal structure of the Gamburtsev Mountains, East Antarctica, from *S*-wave receiver functions and Rayleigh wave phase velocities, *Earth planet. Sci. Lett.,* **300,** 395–401.

Hansen, S.E. *et al.*, 2014. Imaging the Antarctic mantle using adaptively parameterized *P*-wave tomography: evidence for heterogeneous structure beneath West Antarctica, *Earth planet. Sci. Lett.,* **408,** 66–78.

Heeszel, D. *et al.*, 2016. Upper mantle structure of central and West Antarctica from array analysis of Rayleigh wave phase velocities, *J. geophys. Res*., submitted.

Huerta, A.D. & Harry, D.L., 2007. The transition from diffuse to focused extension: Modeled evolution of the West Antarctic Rift system, *Earth planet. Sci. Lett.,* **255,** 133–147.

Huybrechts, P., Denton, G.H.E. & Marchant, D.R.E., 1993. Glaciological modelling of the late Cenozoic East Antarctic ice sheet; stability or dynamism?, *Geogr. Ann. Ser. A Phys. Geogr.,* **75,** 221–238.

Jordan, T.A., Ferraccioli, F., Vaughan, D.G., Holt, J.W., Corr, H., Blankenship, D.D. & Diehl, T.M., 2010. Aerogravity evidence for major crustal thinning under the Pine Island Glacier region (West Antarctica), *Bull. geol. Soc. Am.,* **122,** 714–726.

Kachingwe, M., Nyblade, A. & Julia, J., 2015. Crustal structure of Precambrian terranes in the southern African subcontinent with implications for secular variation in crustal genesis, *Geophys. J. Int.,* **202,** 533–547.

Karner, G.D., Studinger, M. & Bell, R.E., 2005. Gravity anomalies of sedimentary basins and their mechanical implications: application to the Ross Sea basins, West Antarctica, *Earth planet. Sci. Lett.,* **235,** 577–596.

Klemperer, S.L., 1988. Crustal thinning and nature of extension in the northern North Sea from deep seismic reflection profiling, *Tectonics,* **7,** 803–821.

Kohnen, H., 1974. The temperature dependence of seismic waves, *J. Glaciol.,* **13,** 144–147.

Larour, E., Morlighem, M., Seroussi, H., Schiermeier, J. & Rignot, E., 2012. Ice flow sensitivity to geothermal heat flux of Pine Island Glacier, Antarctica, *J. geophys. Res.,* **117**(F4), doi:10.1029/2012JF002371.

Lawrence, J.F., Wiens, D., Nyblade, A., Anandakrishnan, S., Shore, P.J. & Voigt, D., 2006. Rayleigh wave phase velocity analysis of the Ross Sea, Transantarctic Mountains, and East Antarctica from a temporary seismograph array, *J. geophys. Res.,* **111,** 1–15.

LeMasurier, W.E., 2008. Neogene extension and basin deepening in the West Antarctic rift inferred from comparisons with the East African rift and other analogs, *Geology,* **36,** 247–250.

LeMasurier, W.E. & Rex, D.C., 1989. Evolution of linear volcanic ranges in Marie Byrd Land, West Antarctica, *J. geophys. Res.,* **94,** 7223–7236.

Ligorría, J.P. & Ammon, C.J., 1999. Iterative deconvolution and receiver-function estimation, *Bull. seism. Soc. Am.,* **89,** 1395–1400.

Lloyd, A. *et al.*, 2015. A seismic transect across West Antarctica: Evidence for mantle thermal anomalies beneath the Bentley Subglacial Trench and the Marie Byrd Land Dome, *J. geophys. Res.,* **120,** 8439–8460.

Lloyd, A.J., Nyblade, A., Wiens, D., Hansen, S.E., Kanao, M., Shore, P.J. & Zhao, D., 2013. Upper mantle seismic structure beneath central East Antarctica from body wave tomography: Implications for the origin of the Gamburtsev Subglacial Mountains, *Geochem. Geophys. Geosyst.,* **14,** 902–920.

Lough, A.C. *et al.*, 2013. Seismic detection of an active subglacial magmatic complex in Marie Byrd Land, Antarctica. *Nat. Geosci.,* **6,** 1031–1035.

Maguire, P.K.H. *et al.*, 2006. Crustal structure of the Northern Main Ethiopian Rift from the EAGLE controlled source survey; a snapshot of incipient lithospheric break-up, in *The Afar Volcanic Province Within the East African Rift System*, pp. 269–291, eds Yirgu, G., Ebinger, C.J. & Maguire, P.K.H., Geological Society, London, Special Publications.

Moores, E.M., 1991. Southwest U.S.-East Antarctic (SWEAT) connection: a hypothesis, *Geology,* **19,** 425–428.

Morgan, P., 1982. Heat flow in rift zones, in *Continental and Oceanic Rifts,* Vol. 8, pp. 107–122, ed. Palmason, G., AGU Geodynmics Series.

Morin, R.H., Williams, T., Henrys, S., Magens, D., Niessen, F. & Hansaraj, D., 2010. Heat flow and hydrologic characteristics at the AND-1B borehole, ANDRILL McMurdo Ice Shelf Project, Antarctica, *Geosphere,* **6,** 370–378.

Mukasa, S.B. & Dalziel, I.W.D., 2000. Marie Byrd Land, West Antarctica: evolution of Gondwana's pacific margin constrained by zircon U-Pb geochronology and feldspar common-Pb isotopic compositions, *Bull. geol. Soc. Am.,* **112,** 611–627.

Müller, R.D., Gohl, K., Cande, S.C., Goncharov, A. & Golynsky, A.V., 2007. Eocene to Miocene geometry of the West Antarctic Rift System, *Aust. J. Earth Sci.,* **54,** 1033–1045.

Nyblade, A. & Pollack, H.N., 1993. A global analysis of heat flow from Precambrian terrains: implications for the thermal structure of Archcan and Proterozoic lithosphere, *J. geophys. Res.,* **98,** 12 207–12 218.

O'Donnell, J.P. & Nyblade, A., 2014. Antarctica's hypsometry and crustal thickness: implications for the origin of anomalous topography in East Antarctica, *Earth planet. Sci. Lett.,* **388,** 143–155.

Parizek, B.R., 2002. Sub-catchment melt and long-term stability of ice stream D, West Antarctica, *Geophys. Res. Lett.,* **29,** 1–4.

Pattyn, F., 2010. Antarctic subglacial conditions inferred from a hybrid ice sheet/ice stream model, *Earth planet. Sci. Lett.,* **295,** 451–461.

Pollack, H.N., Hurter, S.J. & Johnson, R., 1993. Heat flow from the earth´s interior: analysis of the global data set. *Rev. Geophys.,* **31,** 267–280.

Pollard, D. & DeConto, R.M., 2009. Modelling West Antarctic Ice Sheet growth and collapse through the past five million years, *Nature,* **458,** 329–332.

Pollard, D., DeConto, R.M. & Nyblade, A., 2005. Sensitivity of Cenozoic Antarctic ice sheet variations to geothermal heat flux, *Glob. Planet. Change,* **49,** 63–74.

Prodehl, C. *et al.*, 1997. The KRISP 94 lithospheric investigation of southern Kenya — the experiments and their main results, *Tectonophysics,* **278,** 121–147.

Reid, I., 1993. Velocity structure of reflective lower crust beneath the Grand Banks of Newfoundland, *J. geophys. Res.,* **98,** 9845–9859.

Reid, I.D., 1994. Crustal structure of a nonvolcanic rifted margin east of Newfoundland, *J. geophys. Res.,* **99,** 15 161–15 180.

Ritzwoller, M.H., Shapiro, N.M., Levshin, A.L. & Leahy, G.M., 2001. Crustal and upper mantle structure beneath Antarctica and surrounding oceans, *J. geophys. Res.,* **106,** 30 645–30 670.

Rudnick, R.L. & Fountain, D.M., 1995. Nature and composition of the continental crust: a lower crustal perspective, *Rev. Geophys.,* **33,** 267–309.

Rychert, C., Fischer, K.M. & Rondenay, S., 2005. A sharp lithosphere-asthenosphere boundary imaged beneath eastern North America, *Nature,* **436,** 542–545.

Schroeder, D.M., Blankenship, D.D., Young, D. & Quartini, E., 2014. Evidence for elevated and spatially variable geothermal flux beneath the West Antarctic Ice Sheet, *Proc. Natl. Acad. Sci. USA,* **2014,** 3–5.

Siddoway, C.S., 2008. Tectonics of the West Antarctic Rift System: new light on the history and dynamics of distributed intracontinental extension, in *Antarctica: A Keystone in a Changing World—Online Proceedings of the 10th ISAES,* Santa Barbara, CA, pp. 91–114.

Stern, T.A. & ten Brink, U.S., 1989. Flexural uplift of the Transantarctic Mountains, *J. geophys. Res.,* **94,** 10 315–10 330.

Storey, B.C., Leat, P.T., Weaver, S.D., Pankhurst, R.J., Bradshaw, J.D. & Kelley, S., 1999. Mantle plumes and Antarctica-New Zealand rifting: evidence from mid-Cretaceous mafic dykes, *J. Geol. Soc. Lond.,* **156,** 659–671.

Stuart, A., Wilson, T.J. & Whittaker, J., 2007. Tectonic history of mid-miocene to present Southern Victoria Land Basin, inferred from seismic stratigraphy, in McMurdo Sound, Antarctica, in *Antarctica: A Keystone in a Changing World—Online Proceedings of the 10th ISAES*, doi:10.3133/of2007-1047.srp049.

Studinger, M., Bell, R.E., Buck, W.R., Karner, G.D. & Blankenship, D.D., 2004. Sub-ice geology inland of the Transantarctic Mountains in light of new aerogeophysical data, *Earth planet. Sci. Lett.,* **220,** 391–408.

ten Brink, U.S. & Taylor, M.H., 2002. Crustal structure of central Lake Baikal: insights into intracontinental rift, *J. geophys. Res.,* **107,** doi:10.1029/2001JB000300.

ten Brink, U.S., Hackney, R.I., Bannister, S., Stern, T.A. & Makovsky, Y., 1997. Uplift of the Transantarctic Mountains and the bedrock beneath the East Antarctic ice sheet, *J. geophys. Res.,* **102,** 27 603–27 621.

Tessensohn, F. & Woörner, G., 1991. *The Ross Sea rift system, Antarctica: structure, evolution and analogues, in Geological Evolution of Antarctica,* pp. 273–277, eds Thompson, M.R.A., Crame, J.A. & Thomson, J.W., Cambridge Univ. Press.

Trey, H., Cooper, A.K., Pellis, G., Della Vedova, B., Cochrane, G., Brancolini, G. & Makris, J., 1999. Transect across the West Antarctic rift system in the Ross Sea, Antarctica, *Tectonophysics,* **301,** 61–74.

Tugume, F., Nyblade, A., Julià, J. & van der Meijde, M., 2013. Precambrian crustal structure in Africa and Arabia: evidence lacking for secular variation. *Tectonophysics,* **609,** 250–266.

Wannamaker, P.E., Stodt, J. & Olsen, S.L., 1996. Dormant state of rifting below the Byrd Subglacial Basin, West Antarctica, implied by magnetotelluric (MT) profiling, *Geophys. Res. Lett.,* **23,** 2983–2986.

Watson, T., Nyblade, A., Wiens, D., Anandakrishnan, S., Benoit, M., Shore, P.J., Voigt, D. & VanDecar, J., 2006. P and S velocity structure of the upper mantle beneath the Transantarctic Mountains, East Antarctic craton, and Ross Sea from travel time tomography, *Geochem. Geophys. Geosyst.,* **7,** 1–17.

Wilson, D., Aster, R., Ni, J., Grand, S., West, M., Gao, W., Baldrigdge, W.S. & Semken, S., 2005. Imaging the seismic structure of the crust and upper mantle beneath the Great Plains, Rio Grande Rift, and Colorado Plateau using receiver functions, *J. geophys. Res.,* **110,** 1–14.

Wilson, D.C., Angus, D., Ni, J.F. & Grand, S.P., 2006. Constraints on the interpretation of S-to-P receiver functions, *Geophys. J. Int.,* **165,** 969–980.

Wilson, D.S. & Luyendyk, B.P., 2009. West antarctic paleotopography estimated at the eocene-oligocene climate transition, *Geophys. Res. Lett.,* **36,** 10–13.

Wilson, T. *et al.*, 2014. The POLENET-ANET integrated GPS and seismology approach to understanding glacial isostatic adjustment and ice mass change in Antarctica, *American Geophysical Union, Fall Meeting 2014,* abstract #G51A-0341.

Winberry, J.P. & Anandakrishnan, S., 2003. Seismicity and neotectonics of West Antarctica, *Geophys. Res. Lett.,* **30,** 3–5.

Winberry, J.P. & Anandakrishnan, S., 2004. Crustal structure of the West Antarctic rift system and Marie Byrd Land hotspot, *Geology,* **32,** 977–980.

Zandt, G. & Ammon, C.J., 1995. Continental crust composition constrained by measurements of crustal Poisson's ratio, *Nature,* **374,** 152–154.

Zandt, G., Myers, S.C. & Wallace, T.C., 1995. Crust and mantle structure across the Basin and Range-Colorado Plateau boundary at 37°N latitude and implications for Cenozoic extensional mechanism, *J. geophys. Res.,* **100,** 10 529–10 548.

## SUPPORTING INFORMATION

Additional Supporting Information may be found in the online version of this paper:

**Appendix:** The plots for the individual stations are shown in the following figures. Explanation for each of the figure panels is the same as in Fig. 2 of the main text.
(http://gji.oxfordjournals.org/lookup/suppl/doi:10.1093/gji/ggv542/-/DC1).

Please note: Oxford University Press is not responsible for the content or functionality of any supporting materials supplied by the authors. Any queries (other than missing material) should be directed to the corresponding author for the paper.